Journal of Materials Chemistry C

ROYAL SOCIETY OF CHEMISTRY

PAPER

View Article Online
View Journal | View Issue

Cite this: J. Mater. Chem. C, 2020, 8, 11581

Single-component conductors based on closed-shell Ni and Pt bis(dithiolene) complexes: metallization under high pressure†

Hadi Hachem,[a] HengBo Cui,[b] Takao Tsumuraya,[c] Reizo Kato,*[b] Olivier Jeannin,[a] Marc Fourmigué*[a] and Dominique Lorcy*[a]

Neutral, closed-shell nickel and platinum bis(dithiolene) complexes are explored as single-component conductors. Four complexes formulated as $[Ni(R\text{-thiazdt})_2]^0$ and $[Pt(R\text{-thiazdt})_2]^0$ (R-thiazdt: 2-alkyl-1,3-thiazoline-2-thione-4,5-dithiolate; R = Me, Et) were obtained by electrocrystallization from the corresponding monoanionic species. Crystal and electronic structures confirm their semi-conducting behavior, and show the presence of a large HOMO–LUMO gap in the ethyl-substituted (R = Et) complexes while the less sterically hindered methyl-substituted ones exhibit higher conductivities and smaller activation energies. Application of high-quality quasi-hydrostatic pressures in the nickel series using a Diamond Anvil Cell (DAC) strongly enhances the conductivity of $[Ni(Me\text{-thiazdt})_2]^0$, up to 166 S cm^{-1} ($E_{act}$ = 0.1 meV) at 19 GPa. On the other hand, the *N*-ethyl derivative, $[Ni(Et\text{-thiazdt})_2]^0$, turns metallic in the low temperature range (<100 K) when the pressure reaches 4.4 GPa, while a further increase of the pressure to 6.9 GPa turns it metallic over the whole temperature range. Pressure dependence of the activation energy for the methyl complex $[Ni(Me\text{-thiazdt})_2]^0$ suggests that a pressure-induced structural transition hinders the metallization. On the other hand, first-principles calculations for high-pressure structures well explain the pressure-dependence of the conducting behavior of the ethyl complex $[Ni(Et\text{-thiazdt})_2]^0$.

Received 17th June 2020,
Accepted 17th July 2020

DOI: 10.1039/d0tc02868a

rsc.li/materials-c

Introduction

The quest for single component conductors, *i.e.* conducting molecular materials based on one single molecule (at variance with prototypical charge transfer salts and ion radical salts), is currently an active research topic, particularly because the absence of any counterion can favor three-dimensional intermolecular interactions with associated 3D Fermi surface. This quest was initially considered using neutral radical species such as spiro-bis(phenalenyl)boron radicals,[1,2] dithiadiazolyl,[3,4] or dithiazolyl radicals.[5] The strong tendency of such radicals to dimerize in the solid state was recently overcome in quinone-bridged bis(dithiazolyl) radicals with an insulator-to-metal transition observed under pressure above 3 GPa.[6] Another broad class of single component conductors is based on the bimolecular association of two tetrathiafulvalene (TTF) moieties, either through coordination of TTF-dithiolate ligands around a metal center,[7–9] or through hydrogen bonding interactions between TTF-catechol moieties[10] or zwitterionic TTF-extended dicarboxylate radical (TED) (Chart 1).[11] All these formally neutral compounds exhibit highly conducting properties attributable to internal charge transfer.

A third class more recently investigated relies on neutral radical gold bis(dithiolene) complexes (Chart 2a).[12] Indeed, the d^8 closed-shell anionic complexes $[Au(dt)_2]^{1-}$ oxidize reversibly to the neutral radical complexes with solid state association often avoiding the typical face-to-face dimerization of π-type radical species. Many such derivatives exhibit semi-conducting properties,[13] but complexes derived from *N*-alkyl-1,3-thiazoline-2-thione-4,5-dithiolate (abbreviated as R-thiazdt), $[Au(R\text{-thiazdt})_2]^{\bullet}$, were shown to become metallic under pressure (for R = Et above 2.1 GPa)[14,15] or even at ambient pressure and temperature for R = Me.[16]

However, the necessity to work with radical complexes to stabilize a metallic state in single component materials has been recently questioned. For example, the presence of a small HOMO–LUMO gap in closed-shell nickel bis(dithiolene) complexes such as the prototypical $[Ni(dmit)_2]^0$ (dmit = 1,3-dithiole-2-thione-4,5-dithiolate),[17] suggested that under pressure, these insulating

[a] Univ. Rennes, CNRS, ISCR (Institut des Sciences Chimiques de Rennes) – UMR 6226, F-35000 Rennes, France. E-mail: marc.fourmigue@univ-rennes1.fr
[b] Condensed Molecular Materials Laboratory, RIKEN, Wako-Shi, Saitama 351-0198, Japan
[c] Priority Organization for Innovation and Excellence, Kumamoto University, Kumamoto 860-8555, Japan

† Electronic supplementary information (ESI) available. CCDC 2008921–2008927. For ESI and crystallographic data in CIF or other electronic format see DOI: 10.1039/d0tc02868a

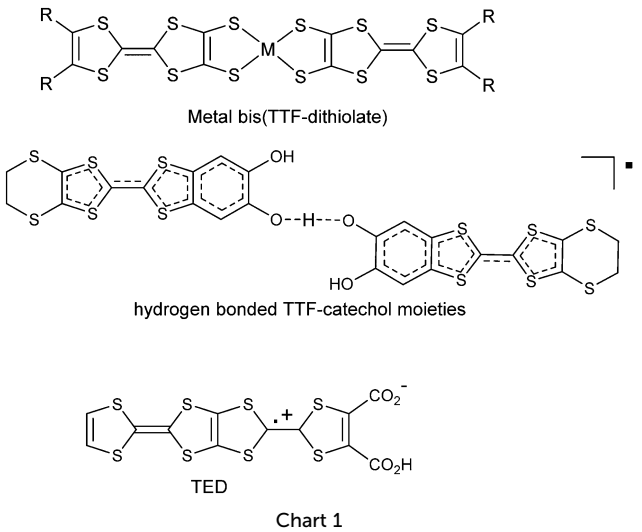

Chart 1

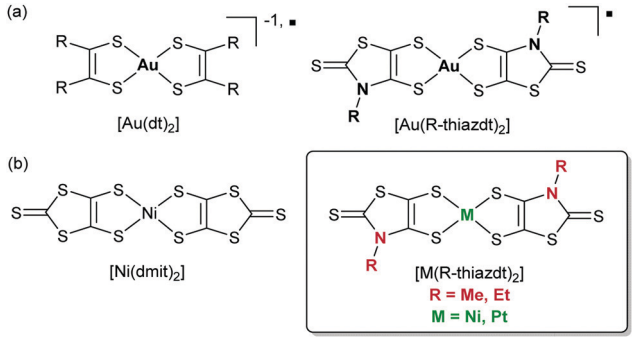

Chart 2

materials[18] could become metallic if the expected increase of band dispersions under pressure could reach a point where the gap would close. This was successfully realized using Diamond Anvil Cell (DAC) on $[Ni(dmit)_2]^0$ itself.[19] It exhibits indeed a low conductivity under ambient pressure at RT, $\sigma_{RT} = 6 \times 10^{-2}$ S cm^{-1} ($E_{act} = 0.14$ eV) but was shown to become essentially metallic above 15.9 GPa. Tight-binding calculations coupled with the interatomic repulsion model and *ab initio* DFT calculations showed that, under high pressures, an overlap of the HOMO and LUMO bands arises, suggesting an internal charge transfer. The calculations also indicated the presence of 2D and 3D Fermi surfaces under those high pressures. Considering the close structural proximity between the dmit and thiazdt ligands and their complexes, and the effective ability of the thiazdt ligand to favor strong overlaps in its gold radical complexes, we wondered if the analogous, closed-shell Nickel or Platinum thiazdt complexes (Chart 2b), namely $[Ni(R\text{-thiazdt})_2]^0$ and $[Pt(R\text{-thiazdt})_2]^0$ (R = Me, Et), would exhibit a similar insulator-to-metal transition under pressure and eventually at lower pressure (if any) than $[Ni(dmit)_2]^0$ itself.

A preliminary investigation showed that a monoclinic phase of the ethyl-substituted complex, mono-$[Ni(Et\text{-thiazdt})_2]^0$ exhibits an activated conductivity with $\sigma_{RT} = 1.4 \times 10^{-2}$ S cm^{-1} and an activation energy of 0.2 eV, but only slightly reduced to 0.17 eV at 1.2 GPa.[20] We described here the preparation of both methyl- and ethyl-substituted complexes with both nickel and platinum, affording four novel phases, a triclinic phase noted tricl-$[Ni(\mathbf{Et}\text{-thiazdt})_2]^0$ together with its platinum analog $[Pt(\mathbf{Et}\text{-thiazdt})_2]^0$, and the corresponding methyl-substituted complexes, $[Ni(\mathbf{Me}\text{-thiazdt})_2]^0$ and $[Pt(\mathbf{Me}\text{-thiazdt})_2]^0$. We demonstrate that the thiazdt ligand allows indeed for the stabilization of a metallic state at limited pressures in these formally closed shell, neutral complexes.

Results and discussion

Syntheses

The general strategy used to form the nickel and platinum dithiolene complexes starting from the cyanoethyl-protected **1-R** proligands (R = Me, Et)[14,21] is outlined in Scheme 1. Treatment of **1-R** (R = Me, Et) with sodium methanolate followed by successive additions of $NiCl_2{\cdot}6H_2O$ and Ph_4PCl, or K_2PtCl_4 and Bu_4NBr led to the corresponding dianionic complexes which, upon purification under air atmosphere, are directly oxidized to the corresponding monoanionic derivatives, $[Ph_4P][Ni(R\text{-thiazdt})_2]$ and $[Bu_4N][Pt(R\text{-thiazdt})_2]$ respectively (R = Me, Et). We also tried to prepare the corresponding Ph_4P^+ salts of the platinum complexes $[Pt(R\text{-thiazdt})_2]^{1-}$ complexes but their purification proved to be very difficult and only a few crystals of $[Ph_4P][Pt(R\text{-thiazdt})_2]$ were isolated (see below). This purification problem was overcome using Bu_4N^+ as counter-ion.

The corresponding neutral complexes were obtained by electrocrystallization of the anionic salts, by analogy with that already described for mono-$[Ni(Et\text{-thiazdt})_2]^0$.[20] Albeit neutral complexes are obtained without incorporation of any counter ion in the structure, we found that the choice of the electrolyte used in the electrocrystallization cell is particularly important to favor a given phase and/or high quality crystals. Indeed, the reported monoclinic phase mono-$[Ni(Et\text{-thiazdt})_2]^0$ had been obtained with Et_4NBr in CH_3CN as electrolyte, but with a few crystals of a triclinic phase that had escaped our attention at that time. The latter triclinic phase tricl-$[Ni(Et\text{-thiazdt})_2]^0$ has been obtained here almost pure when using Et_4NPF_6 or Me_4NPF_6 in CH_3CN as electrolyte, with the best crystals in the presence of Et_4NPF_6. High quality crystals of the neutral methyl Ni complex $[Ni(Me\text{-thiazdt})_2]^0$ were isolated from Ph_4PCl in CH_2Cl_2/MeOH (7 : 3) as electrolyte. The neutral platinum complexes $[Pt(Me\text{-thiazdt})_2]^0$ and $[Pt(Et\text{-thiazdt})_2]^0$ were obtained from

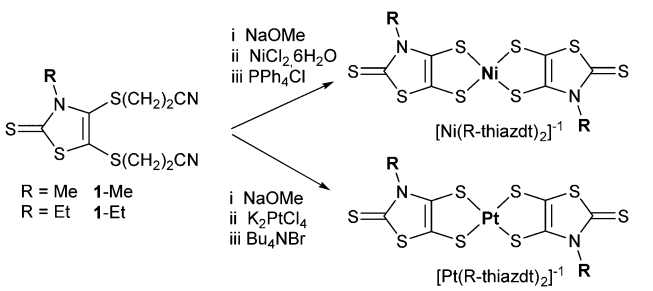

Scheme 1 Synthetic route toward monoanionic nickel bis(dithiolene), $[Ph_4P][Ni(R\text{-thiazdt})_2]$ and platinum bis(dithiolene) $[Bu_4N][Pt(R\text{-thiazdt})_2]$ complexes (R = Me, Et).

Bu_4NBF_4 in respectively CH_2Cl_2/CH_3CN (3/7) or pure CH_3CN. Before analyzing the solid-state properties of these complexes, their electro- and spectro-chemical properties will be described.

Solution properties

The redox properties of these four anionic complexes have been analyzed by cyclic voltammetry in CH_2Cl_2 using NBu_4PF_6 as supporting electrolyte while the UV-Vis-NIR absorption properties of the radical anion species, were measured in CH_2Cl_2 at room temperature. Spectro-electrochemical experiments give access to the absorption properties of the neutral species generated at the electrode, however without possibility to evaluate the corresponding absorption coefficients, due to partial precipitation of the insoluble neutral species. A representative example is given in Fig. 1 for $[Bu_4N][Pt(Et\text{-}thiazdt)_2]$ while all redox potentials, maximum absorption wavelengths and absorption coefficients (on anionic complexes only) are collected in Table 1.

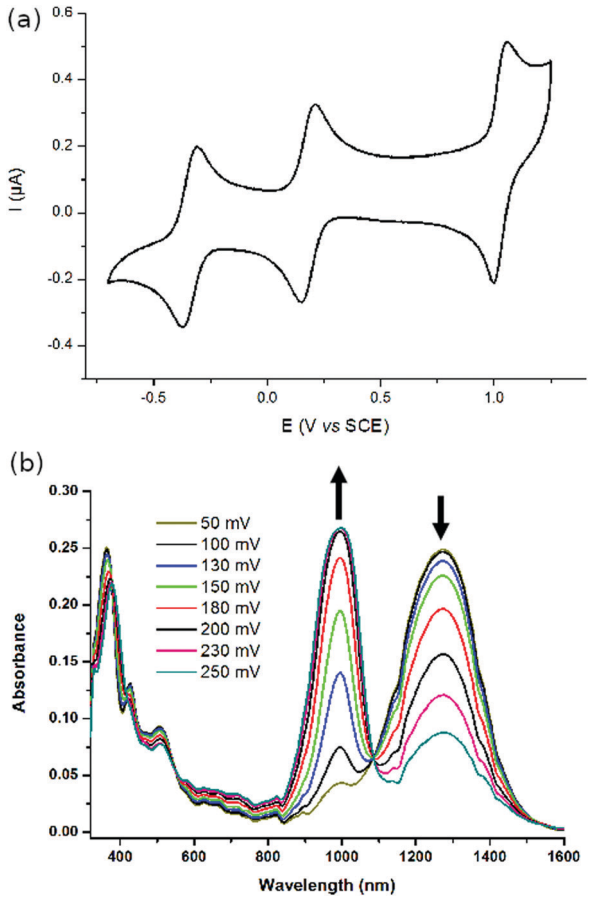

Fig. 1 (a) Cyclic voltammetry (b) and UV-Vis-NIR monitoring of the electrochemical oxidation of $[Bu_4N][Pt(Et\text{-}thiazdt)_2]$.

The properties of the nickel complexes compare with those described earlier.[20] The neutral Pt complex $[Pt(Et\text{-}thiazdt)_2]$ has been reported by Arca *et al.* in low yields from the sulfuration of ethyl-2-thioxothiazolidine-4,5-dione with Lawesson's reagent in the presence of $PtCl_2$.[22] Its structure was not reported but its redox properties, which compare indeed with those obtained here from the soluble monoanionic salt. However, as noticed earlier for the $[Ni(Et\text{-}thiazdt)_2]$,[20] the $[Pt(Et\text{-}thiazdt)_2]$ exhibits three redox processes (Fig. 1a). This third process, not mentioned earlier, is associated to the oxidation of the neutral species into the cation radical one (Table 1). For the *N*-methyl complexes this third redox process is not observed presumably due to a lower solubility of these derivatives compared to the *N*-Et ones and also due to strong adsorption phenomena.

The UV-vis-NIR spectroscopic investigations carried out on the four complexes allowed us to determine the absorption maxima (λ_{max}) of the lowest energy NIR electronic transitions for the monoanionic species as well as the neutral complexes. As expected, a hypsochromic shift is observed for the absorption band at low energies when going from the monoanion to the neutral species. The nature of the alkyl group has no significant influence on the wavelength of the NIR absorption band. On the other hand, the nature of the metal induces discrepancies. The Ni complexes present slightly red shifted λ_{max} by 20–28 nm for the monoanions as well as for the neutral complexes. Moreover, the extinction coefficients for the Pt monoanions are 1.5 times higher than those of the Ni complexes.

Solid state properties

Good quality single crystals for X-ray diffraction studies were obtained for the monoanionic nickel complex $[PPh_4][Ni(Me\text{-}thiazdt)_2]$ as needles. A minor phase co-crystallizing in the form of thin plates was found to be a CH_2Cl_2 solvate. Note that the ethyl analog $[Ph_4P][Ni(Et\text{-}thiazdt)_2]$ was already described[20] while both platinum salts $[NBu_4][Pt(R\text{-}thiazdt)_2]$ (R = Me, Et) could not be obtained in the form of high quality crystals. As mentioned above, a few crystals of $[Ph_4P][Pt(Et\text{-}thiazdt)_2]$ obtained

Table 1 Redox potentials (E in V *vs.* SCE), absorption maxima λ_{max} (nm) and molar extinction coefficients ε (M^{-1} cm^{-1}) for the NIR absorptions of the $[Ni(R\text{-}thiazdt)_2]$ and $[Pt(R\text{-}thiazdt)_2]$ (R = Me, Et) complexes

	$E_1^{-2/-1}$	$E_2^{-1/0}$	E_3	λ_{max} (ε) (nm, M^{-1} cm^{-1}) Anion radical	Neutral	Ref.
$[Ni(Me\text{-}thiazdt)_2]$	−0.33	+0.18/−0.01[a]	—	1278 (20 880)	1012	This work
$[Ni(Et\text{-}thiazdt)_2]$	−0.37	+0.17	1.12	1280 (21 000)	1022	20
$[Pt(Me\text{-}thiazdt)_2]$	−0.30	+0.23/0.07[a]	—	1256 (33 920)	992	This work
$[Pt(Et\text{-}thiazdt)_2]$	−0.31	+0.21	1.04/0.94[a]	1260 (32 190)	994	This work
	−0.797[b]	−0.276[b]	—	1252[c]	1010[d]	22

$E = (E_{pa} + E_{pc})/2$. [a] E_{pa}/E_{pc}: anodic and cathodic peak potentials. [b] Data reported in CH_2Cl_2 *vs.* Fc^+/Fc couple. [c] In CH_2Cl_2. [d] In toluene.

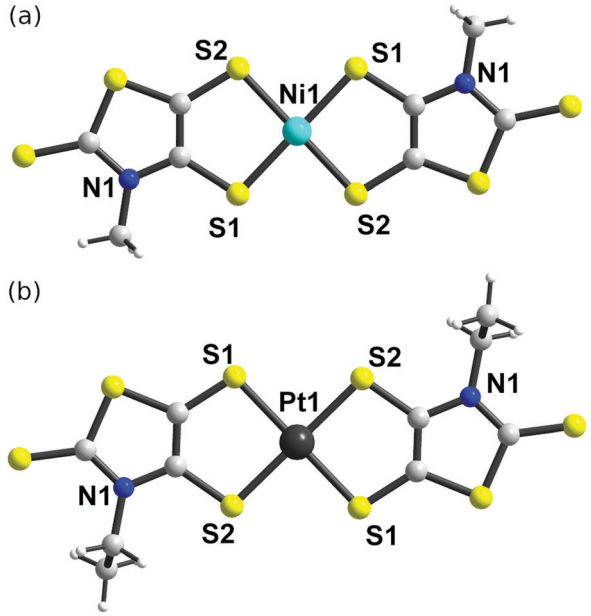

Fig. 2 Molecular view of the anion radical species $[Ni(Me\text{-}thiazdt)_2]^{1-}$ in $[Ph_4P][Ni(Me\text{-}thiazdt)_2]$ (top) and $[Pt(Et\text{-}thiazdt)_2]^{1-}$ in $[Ph_4P][Pt(Et\text{-}thiazdt)_2]$ (bottom).

as a toluene solvate phase could only be characterized by X-ray diffraction studies. The non-solvated salt $[Ph_4P][Ni(Me\text{-}thiazdt)_2]$ crystallizes in the monoclinic system, space group $C2/c$, with the nickel atom on an inversion center (Fig. 2a) and the phosphorous of the Ph_4P^+ cation on a two-fold axis. Pertinent bond distances and angles are collected in Table 2.

In the crystal, the anion radical $[Ni(Me\text{-}thiazdt)_2]^{1-}$ species organize into uniform stacks running along the b axis, further interacting sideways along a. These ab anionic layers are alternating along c with Ph_4P^+ layers (Fig. S1, ESI†). The shortest intermolecular S···S contacts exceed 3.96 Å, a large distance which lets us infer very weak magnetic interactions between the $S = 1/2$ radical species. The cocrystallization of this salt with its CH_2Cl_2 solvate prevented us to measure the actual magnetic susceptibility and its temperature evolution. The minor solvate phase crystallizes in the orthorhombic system, space group $P2_1ca$, with anion, cation and CH_2Cl_2 molecule in general position. The $[Ni(Me\text{-}thiazdt)_2]^{1-}$ moiety exhibits weak deviation from planarity and is organized into stacks running along the b axis, with again very limited interactions within the stacks (Fig. S2, ESI†). Interestingly, the monoanionic $[Ni(Me\text{-}thiazdt)_2]^{1-}$ complex in both structures adopts a *trans*, ordered configuration while, when crystallized with the Et_4N^+ counter ion, this unsymmetrical dithiolene ligand was found to be disordered on two positions.[21]

Table 2 Intramolecular bond distances within the anionic and neutral complexes $[M(R\text{-}thiazdt)_2]^{1-,0}$ M = Ni, Pt and R = Me, Et

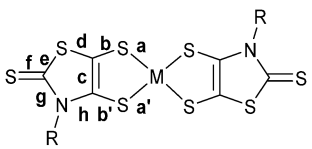

	a	a'	b	b'	c
Nickel complexes					
$[Ni(Me\text{-}thiazdt)_2]^{1-}$ [a]	2.1689(12)	2.1709(17)	1.709(6)	1.727(5)	1.348(7)
$[Ni(Me\text{-}thiazdt)_2]^{1-}$ [b]	2.176(3)	2.174(3)	1.71(1)	1.747(9)	1.32(1)
$[Ni(Me\text{-}thiazdt)_2]^{0}$	2.1457(10)	2.1619(11)	1.676(4)	1.700(4)	1.396(5)
$[Ni(Et\text{-}thiazdt)_2]^{1-}$ [c]	2.1778(6)	2.1560(6)	1.722(2)	1.712(2)	1.356(3)
tricl-$[Ni(Et\text{-}thiazdt)_2]^{0}$	2.157(1)	2.156(1)	1.679(3)	1.697(2)	1.389(4)
mono-$[Ni(Et\text{-}thiazdt)_2]^{0}$ [c]	2.1580(6)	2.1577(6)	1.685(2)	1.700(2)	1.388(3)
Platinum complexes					
$[Pt(Me\text{-}thiazdt)_2]^{0}$	2.249(5)	2.271(5)	1.656(17)	1.710(19)	1.39(3)
$[Pt(Et\text{-}thiazdt)_2]^{1-}$ [a]	2.2705(13)	2.2853(13)	1.701(5)	1.732(6)	1.331(8)
$[Pt(Et\text{-}thiazdt)_2]^{0}$	2.261(11)	2.264(8)	1.686(11)	1.708(11)	1.348(12)

	d	e	f	g	h
Nickel complexes					
$[Ni(Me\text{-}thiazdt)_2]^{1-}$ [a]	1.739(5)	1.727(6)	1.672(6)	1.370(7)	1.393(7)
$[Ni(Me\text{-}thiazdt)_2]^{1-}$ [b]	1.759(9)	1.76(1)	1.672(9)	1.35(1)	1.40(1)
$[Ni(Me\text{-}thiazdt)_2]^{0}$	1.727(4)	1.744(4)	1.649(4)	1.362(5)	1.373(5)
$[Ni(Et\text{-}thiazdt)_2]^{1-}$ [c]	1.739(2)	1.735(3)	1.664(3)	1.362(4)	1.398(3)
tricl-$[Ni(Et\text{-}thiazdt)_2]^{0}$	1.733(3)	1.750(3)	1.640(4)	1.366(4)	1.376(4)
mono-$[Ni(Et\text{-}thiazdt)_2]^{0}$ [c]	1.733(2)	1.755(2)	1.640(2)	1.372(3)	1.378(3)
Platinum complexes					
$[Pt(Me\text{-}thiazdt)_2]^{0}$	1.734(16)	1.71(2)	1.668(18)	1.35(2)	1.39(2)
$[Pt(Et\text{-}thiazdt)_2]^{-1}$ [a]	1.754(5)	1.726(8)	1.668(6)	1.353(9)	1.406(6)
$[Pt(Et\text{-}thiazdt)_2]^{0}$	1.740(11)	1.742(11)	1.639(11)	1.366(13)	1.379(12)

[a] As Ph_4P^+ salt. [b] As Ph_4P^+ salt, CH_2Cl_2 solvate. [c] From ref. 20.

The Ph_4P^+ salt of the Pt complex, namely $[Ph_4P][Pt(Et\text{-}thiazdt)_2]\cdot$ toluene, crystallizes as toluene solvate in the monoclinic system, space group $C2/c$ with the Pt atom on an inversion center and the phosphorous of the Ph_4P^+ cation on a two-fold axis (Fig. 2b). The molecules organize into alternating layers of cations and anions in the *ac* plane (Fig. S3, ESI†). The monoanionic $[Pt(Et\text{-}thiazdt)_2]^{1-}$ complex is obtained also as the *trans* isomer.

The four novel neutral complexes, $[Ni(Me\text{-}thiazdt)_2]$, tricl-$[Ni(Et\text{-}thiazdt)_2]$, $[Pt(Me\text{-}thiazdt)_2]$ and $[Pt(Et\text{-}thiazdt)_2]$ prepared by electrocrystallization (see above) were isolated as tiny black crystals at the anode. They will be abbreviated as **NiMe**, tricl-**NiEt**, **PtMe** and **PtEt** in the following. Intramolecular bond distances are collected in Table 2. Their evolutions from the monoanionic to the neutral species within the metallacycle show a shortening of the C–S bonds and a lengthening of the C=C bond. Such geometrical changes are recurrently observed upon oxidation of anionic complexes to the neutral species and are the signature of the non-innocent character of the dithiolene ligand which tends to adopt a dithioketone form upon oxidation. Less pronounced modifications are observed on the outer heterocycle ring with however a noticeable shortening of the exocyclic C=S bond. All neutral complexes crystallize on inversion center as the *trans* isomers, all of them in the $P\bar{1}$ space group, except **PtMe** which is found to crystallize in the monoclinic $P2_1/c$ space group. The two *N*-ethyl complexes, tricl-**NiEt** and **PtEt** are isostructural.

A common trend within the four structures is the formation of uniform, non-dimerized stacks with the complexes interacting sideways (Fig. 3). We have reported recently that dimerization within the stacks of such complexes was most often a consequence of overlap interactions between open-shell species, as found indeed in several neutral, but radical gold dithiolene complexes. Among the few reported neutral platinum dithiolene complexes, only $[Pt(edt)_2]$ is actually dimerized,[23] while $[Pt(dddt)_2]$,[24] $[Pt(tfd)_2]$[25] and $[Pt(timdt)_2]$[26] crystallize into uniform stacks. The overlap mode between two neighboring complexes within the stacks is shown in Fig. 4.

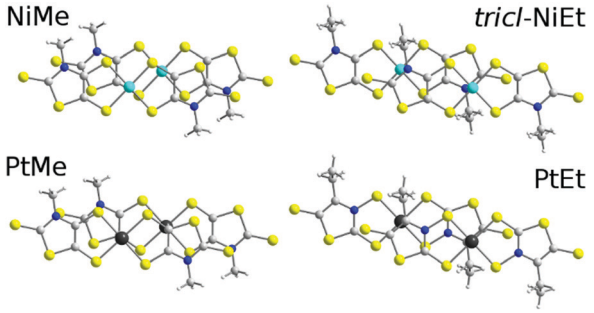

Fig. 4 Projection views of the overlap between neighboring complexes within the stacks in the four complexes.

We note that the presence of the bulkier ethyl substituent induces a more pronounced longitudinal slip than in the *N*-methyl derivatives. The plane-to-plane distances are comparable and quite large in the four complexes, *i.e.* 3.55, 3.58, 3.61 and 3.58 Å in **NiMe**, tricl-**NiEt**, **PtMe**, and **PtEt** respectively, if compared to twice the sulfur van der Waals radius, *i.e.* 3.60 Å.

The shortest intermolecular lateral S···S contacts identified between neighboring stacks are found in the *N*-methyl complexes, at 3.48 Å in **NiMe** and 3.39 Å in **PtMe** while they exceed 3.7–3.80 Å in the *N*-ethyl complexes tricl-**NiEt** and **PtEt**. All structures offer also the possibility for an interaction between these layers involving a S···S contact between the outer C=S moieties of the complexes. They are particularly short in the *N*-ethyl complexes, 3.29(2) Å in tricl-**NiEt** and 3.29(1) Å in **PtEt** but exceed 3.61 Å in the *N*-methyl ones **NiMe** and **PtMe**. This is in sharp contrast with what was observed for the analogous gold complexes **AuMe** and **AuEt**, where the shortest distance between the exocyclic sulfur atoms was found for the **AuMe**[16] and not for **AuEt**.[14] From these contrasted observations, it appears that intermolecular interactions within the stacks are most probably quite weak, perhaps stronger in the *N*-methyl complexes which exhibit a more favorable overlap, while few short S···S contacts can be also identified between stacks.

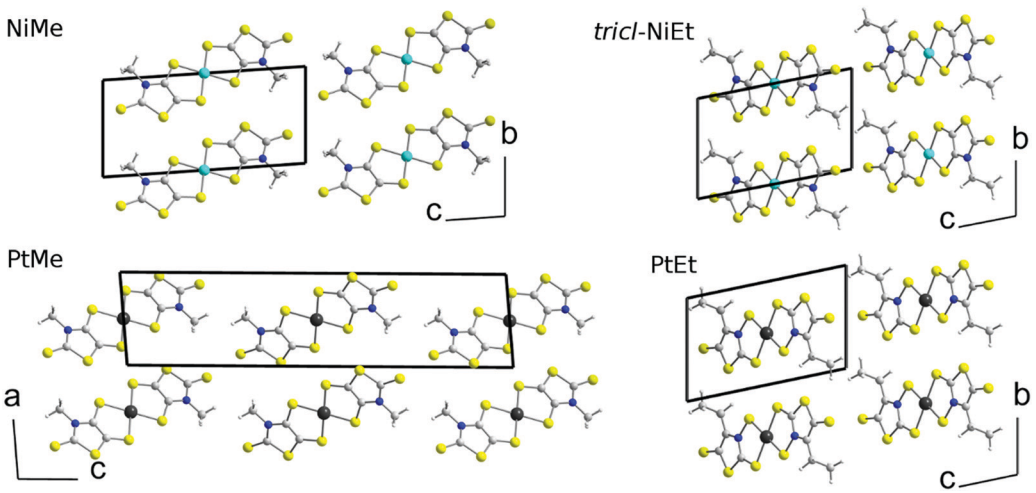

Fig. 3 Projection views of the unit cells of the neutral complexes.

Table 3 Electronic properties (conductivity, activation energy, band gap) of the neutral complexes

Complex	σ_{RT} at 1 bar (S cm^{-1})	Exp. E_{act} (eV)	Calcd[b] direct band gap (eV)
[Ni(Me-thiazdt)$_2$]	5×10^{-2}	0.11	0.27
tricl-[Ni(Et-thiazdt)$_2$]	4.3×10^{-4}	0.21	0.53
mono-[Ni(Et-thiazdt)$_2$]	1.4×10^{-2}[a]	0.20[a]	0.55
[Pt(Me-thiazdt)$_2$]	1.6×10^{-2}	0.16	0.28
[Pt(Et-thiazdt)$_2$]	2.9×10^{-3}	0.18	0.43

[a] From Ref. 20. [b] Tight binding calculations.

The conductivity of the four complexes and its temperature dependence reflect these observations. As shown in Table 3, the four complexes exhibit a semiconducting behavior in the whole temperature range, with a higher conductivity and smaller activation energy for the *N*-methyl complexes.

Band structures calculations (tight-binding) were performed on these series of four neutral complexes to rationalize their transport properties, in relation with their actual solid-state structure (Fig. 5). We note for the four structures very limited band dispersion, in accordance with the structural analysis developed above. This band dispersion is negligible in the *N*-ethyl complexes, a direct consequence of the weaker, shifted overlap within the stacks. Besides, the direct gap between the HOMO and LUMO bands ranges from 0.31–0.33 eV in the *N*-methyl complexes **NiMe** and **PtMe** while it exceeds 0.60 eV in the *N*-ethyl complexes.

Transport properties and electronic calculations can be compared here with those reported recently for neutral [Ni(dmit)$_2$], with $\sigma_{RT} = 1.6 \times 10^{-2}$ S cm^{-1} and $E_{act} = 0.14$ eV at ambient pressure. [Ni(dmit)$_2$] was shown to become essentially metallic above 8.3 GPa, a striking result which lets us infer a similar behavior in the complexes reported here, and particularly in the most conductive one, *i.e.* **NiMe**. The evolution of its conductivity under high pressure was accordingly determined in a diamond anvil cell (DAC), as reported for [Ni(dmit)$_2$].[19] For comparison purposes, a similar investigation has been made on the tricl-**NiEt** phase.

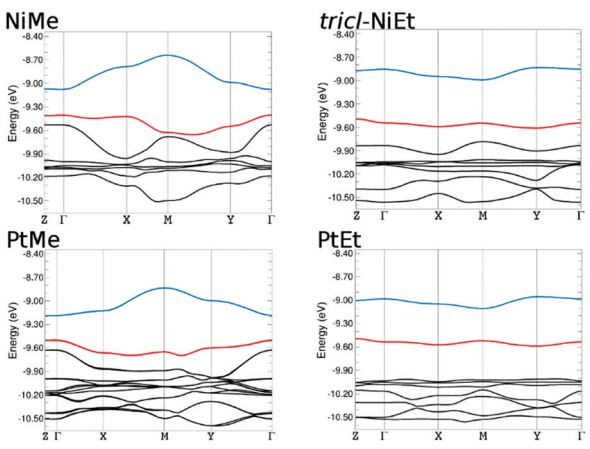

Fig. 5 Calculated band structure for the four complexes, determined by tight-binding methods, where Γ = (0,0,0), X = (1/2,0,0), Y = (0,1/2,0), Z = (0,0,1/2), and M = (1/2,1/2,1/2). The HOMO and LUMO bands are highlighted respectively in red and blue.

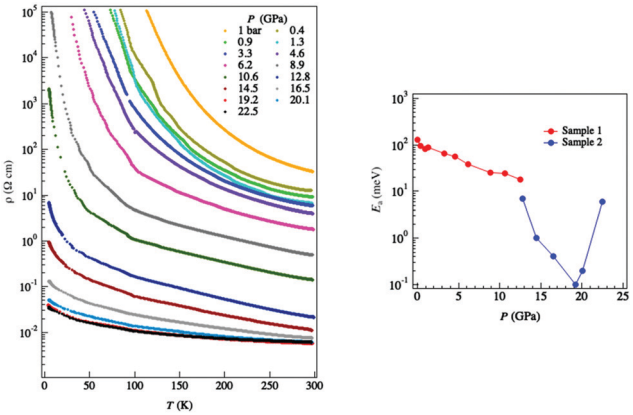

Fig. 6 Temperature dependence of the resistivity of **NiMe** as a function of temperature, and at different pressures between 1 bar and 22.5 GPa (left). Pressure dependence of the activation energy of **NiMe** (right).

Although a diamond anvil cell (DAC) is very useful for high-pressure measurements, the pressure generated by a DAC tends to be anisotropic and its effect is often different from that of hydrostatic pressure. The DAC technique developed by some of us can generate high-quality quasi-hydrostatic pressures and was applied to the present **NiMe** and tricl-**NiEt** systems, as shown in Fig. 6 and 7.

When the pressure is increased from 1 bar to 22.5 GPa in **NiMe** (Fig. 6), the room temperature conductivity is increased by 5 orders of magnitude (up to σ_{RT} = 166 S cm^{-1}) and the activation energy is reduced down to 0.1 meV at 19 GPa. However, even at the highest pressures, **NiMe** keeps its semiconducting nature. Note also that the evolution of the activation energy (Fig. 6 right) is not regular, indicating that a structural transition might have taken place already at 13 GPa. As a consequence, the ambient pressure structure cannot really be used as a starting model for anticipating the evolution of the band structure of **NiMe** under high pressure.

The temperature dependence of the conductivity of the platinum complexes was also investigated. The resistivity measurements on

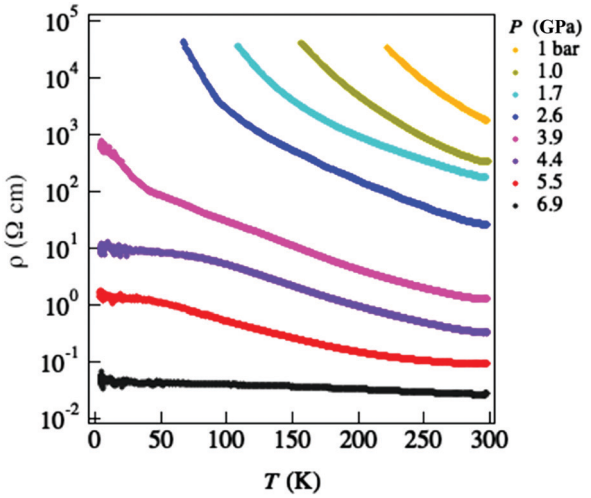

Fig. 7 Pressure dependence of resistivity of tricl-**NiEt** between 1 bar and 6.9 GPa.

PtMe show a semiconducting behavior at ambient pressure, with a room temperature conductivity of 1.66×10^{-2} S cm^{-1} with an activation energy of 0.16 eV (Fig. S4, ESI†) which is the same order of magnitude of the **NiMe** analog. The calculated activation energy is 0.16 eV which goes in line with the predicted value from the band structure calculation (Fig. 5). The very small size of the samples prevented the realization of resistivity measurements under pressure.

As anticipated above from the crystal structures, the room temperature conductivity of **PtEt** is smaller and amounts to $\sigma_{RT} = 2.9 \times 10^{-3}$ S cm^{-1} with an activation energy of 0.18 eV. The pressure dependence of the conductivity was investigated here, showing that the semiconducting state was maintained even at 12 GPa, with $\sigma_{RT}(p = 12$ GPa) at 5.8 S cm^{-1} and $E_{act}(p = 12$ GPa) at 0.058 eV (Fig. S5, ESI†). This behavior contrasts with that of the isostructural **NiEt** complex which turns metallic already above 4.4 GPa.

To understand the evolutions of the structural and electronic properties of **NiMe** under pressure, structural optimization with first-principles DFT calculation was performed by keeping crystal symmetry (constraint for space group) as the experimental structure at ambient pressure (Fig. 8). The optimized structure at 4 GPa predicts a semimetallic band structure (Fig. 8b), while experiments show an insulating behavior. The full clarification of structural properties of **NiMe** above 4 GPa with a possible phase transition inferred from the pressure dependence of the activation energy (Fig. 8b) is left for future studies.

At variance with **NMe**, a quasi-metallic behavior is already observed in tricl-**NiEt** (Fig. 7) in the low temperature range (<100 K) when the pressure reaches 4.4 GPa, while a further increase of the pressure to 6.9 GPa realized a quasi-metallic behavior over the whole temperature range, with a room temperature conductivity reaching 250 S cm^{-1}. Note that this successful metallization process is observed here at a notably lower pressure (4.4 GPa) than in the reported $[Ni(dmit)_2]^0$ (8.3 GPa).[19] First-principles calculations were also performed on the tricl-**NiEt** complex. As shown in Fig. 9a, the calculated ambient-pressure band structure shows insulating character with an indirect band gap of 0.3 eV. The cell parameters and internal coordinates of tricl-**NiEt** complex were then relaxed at several given pressures with a non-local electron correlation functional of vdW-DF2.[27]

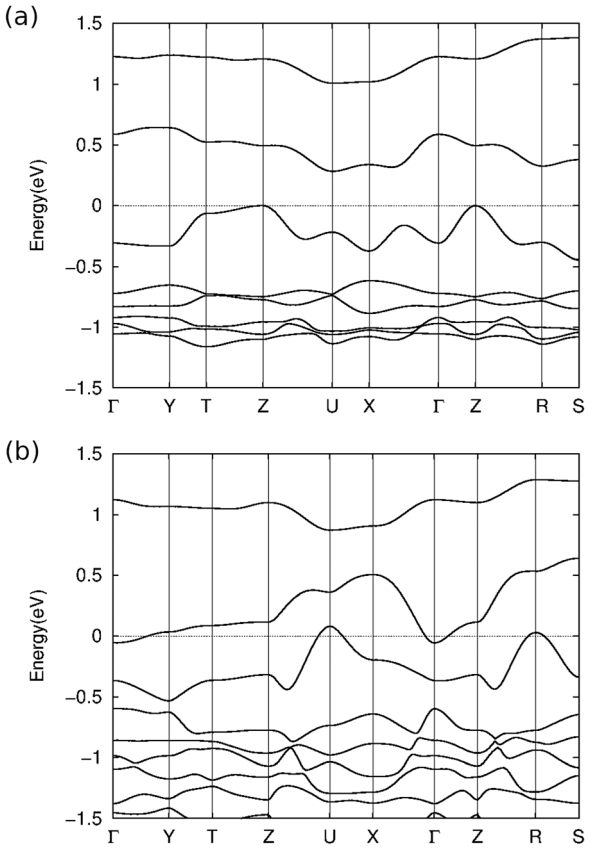

Fig. 9 First-principles band structure of tricl-**NiEt** at (a) ambient pressure and (b) 6 GPa. See Fig. S6 (ESI†) for the calculated band structures at 2, 4 and 8 GPa and Fig. S7 (ESI†) for details of the first Brillouin zone of the optimized structure of 6 GPa. The dotted lines at energy = 0 eV in (a) and (b) represent the top of the valence bands and Fermi energy respectively.

The electronic structure is changed upon applying pressure and the calculated band structure at 6 GPa (Fig. 9b) confirms indeed the appearance of a metallic state, with the Fermi level cutting the HOMO and LUMO bands at different k vectors in the reciprocal space, where 3D electron pockets around the Γ-point and 2D cylindrical hole Fermi surface surrounding the U and R points are found (Fig. 10c). This result agrees with the experimental results shown in Fig. 7 which indicates the conducting

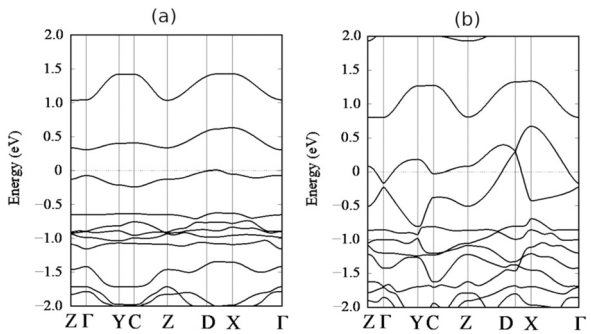

Fig. 8 Band structure of **NiMe** calculated with GGA for the structures at (a) ambient pressure and (b) 4 GPa. The dotted lines at energy = 0 eV in (a) and (b) represent the top of the valence bands and Fermi energy respectively.

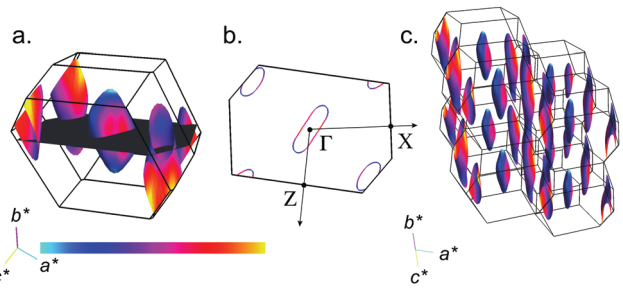

Fig. 10 Calculated Fermi surface of tricl-**NiEt** at 6 GPa. (a) First Brillouin zone; (b) 2D plane of the Fermi surface perpendicular to the b^*-axis containing the Γ-point, and (c) Bird's view of the Fermi surface of 2 × 2 × 2 cell of the first Brillouin zone. Color bar indicates Fermi velocity. The figures are plotted using FermiSurfer 2.1.0.[28]

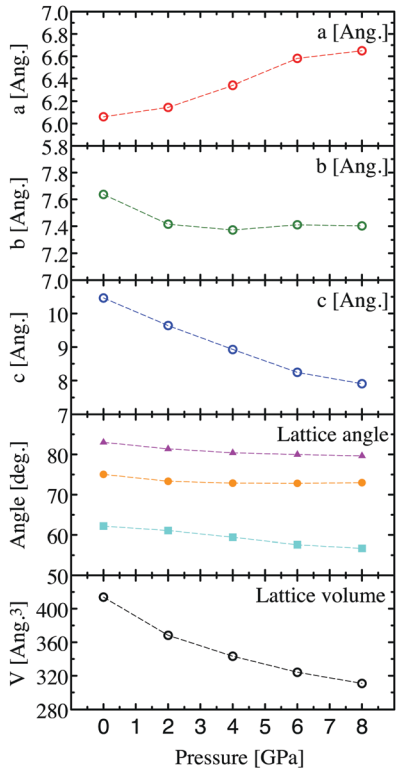

Fig. 11 Pressure dependence of DFT optimized lattice parameters in tricl-**NiEt**. The structural optimization is performed on the basis of exchange–correlation functional of vdW-DF2. Solid circles, triangles, and squares are lattice angles α, β, and γ, respectively.

behavior at 6 GPa. Next, analysis of the changes in the structures under pressure is performed.

The calculated evolution of the crystal structure of tricl-**NiEt** under pressure is shown in Fig. 11 and 12 (see Tables S1–S5 in ESI† for crystallographic data at different pressures).

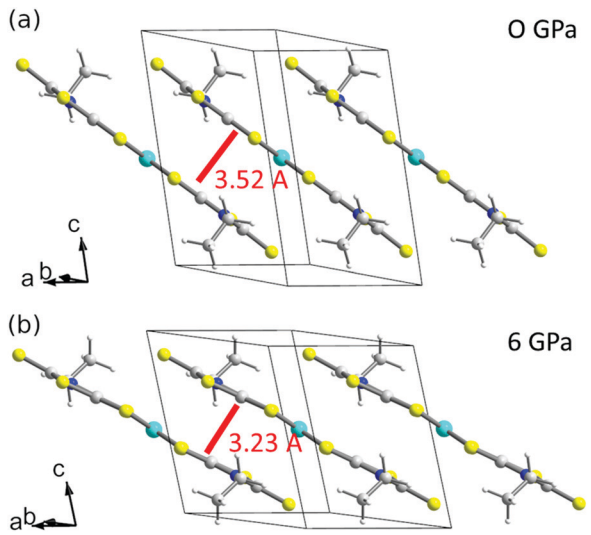

Fig. 12 Crystal structures of tricl-**NiEt** at (a) ambient pressure and, (b) 6 GPa. The structural parameters at 6 GPa are obtained from the structural optimization with first-principles calculation based on the exchange–correlation functional of vdW-DF2 (see Table S4, ESI†).

With increasing pressure, the lattice constant a increases, which is associated with an inclination of $[Ni(Et\text{-}thiazdt)_2]$ molecules along the a axis. This is also linked to the significant decrease of the lattice constant c. It should be noted that the ethyl group rotates around the N–C bond cooperating with the lattice compression along the c direction as shown in Fig. 12. When the band structure becomes that of a metallic state, the intermolecular overlap of the Et-thiazdt ligand becomes more efficient with the π–π stacking distance shorter than 3.5 Å (Fig. 12 and Fig. S8, ESI†). This results in the increased bandwidth of the conduction bands (especially LUMO bands along the Γ–X direction).

Conclusions

Four neutral, formally closed-shell, Ni and Pt complexes formulated as $[Ni(R\text{-}thiazdt)_2]^0$ and $[Pt(R\text{-}thiazdt)_2]^0$ (R-thiazdt: 2-alkyl-1,3-thiazoline-2-thione-4,5-dithiolate; R = Me, Et) were obtained by electrocrystallization from the corresponding monoanionic species. Their crystal and electronic structures confirm their semiconducting behavior, and show the presence of a large HOMO–LUMO gap in the ethyl (R = Et) substituted complexes while the less sterically hindered methyl-substituted ones exhibit higher conductivities and smaller activation energies. Application of high-quality quasi-hydrostatic pressures in the nickel series using a Diamond Anvil Cell (DAC) strongly enhances the conductivity of $[Ni(Me\text{-}thiazdt)_2]^0$ (**NiMe**) up to 166 S cm^{-1} (E_{act} = 0.1 meV) at 19 GPa. On the other hand, the *N*-ethyl derivative, $[Ni(Et\text{-}thiazdt)_2]^0$ (tricl-**NiEt**) turns metallic in the low temperature range (<100 K) when the pressure reaches 4.4 GPa, while a further increase of the pressure to 6.9 GPa turns it metallic over the whole temperature range. As for **NiMe**, the discrepancy between the first-principles calculations predicting metallization under pressure and resistivity measurements probably originates from a possible structural transition under pressure. In tricl-**NiEt**, on the other hand, a favorable situation for metallization is highlighted here, associated with the presence of an indirect gap in the semiconducting regime. At higher pressures, the gap closing is then observed at different k vectors, leading to the semi-metallic Fermi surface. Remarkably, the presence of the bulkier ethyl substituent does not hinder the metallization, which expands possible molecular design for single-component molecular conductors based on such small, non-radical, molecular complexes.

Experimental

General

Chemicals and materials from commercial sources were used without further purification. All the reactions were performed under an argon atmosphere. Melting points were measured on a Kofler hot-stage apparatus and are uncorrected. Mass spectra were recorded by the Centre Régional de Mesures Physiques de l'Ouest, Rennes. Methanol, acetonitrile and dichloromethane were dried using Inert pure solvent column device. CVs were carried out on a 10^{-3} M solution of complex in CH_2Cl_2 with NBu_4PF_6 0.1 M. Potentials were measured *versus* Saturated

Calomel Electrode (SCE). The spectroelectrochemical setup was performed in CH_2Cl_2 with Bu_4NPF_6 0.2 M using a Pt grid as the working electrode, a Pt wire as the counter electrode and SCE reference electrode. A Shimatzu 3600 spectrophotometer was employed to record the UV-vis-NIR spectra. The proligands **1**-Me,[21] **1**-Et,[14] and the Ni complex[14] $[Ph_4P][Ni(Et\text{-}thiazdt)_2]$ were prepared as previously reported. Elemental analyses were performed at Institut de Chimie des Substances Naturelles (CNRS, Gif/Yvette, France)

$[PPh_4][Ni(Me\text{-}thiazdt)_2]$. Under inert atmosphere, a solution of Na (35 mg, 1.5 mmol) in MeOH (20 mL) was added to the proligand **1**-Me (150 mg, 0.5 mmol). After complete dissolution, the solution was stirred at room temperature for 30 min. Then a solution of $NiCl_2{\cdot}6H_2O$ (60 mg, 0.25 mmol) in MeOH (5 mL) was added, followed 6 hours later by the addition of PPh_4Br (210 mg, 0.5 mmol). After stirring for 15 h, the formed reddish precipitate was filtered and recrystallized in the air from CH_2Cl_2/MeOH 20/80 to afford the monoanion complex $[PPh_4][Ni(Me\text{-}thiazdt)_2]$ as dark red crystals. Yield: 48% (94 mg); m.p. = 190 °C. HRMS (ESI) calcd for $[C_{10}H_{10}N_2S_4{}^{58}Ni^{80}Se_4]^-$: 663.57466. Found: 663.5737. Elem. anal. calcd for $C_{32}H_{26}N_2NiPS_8$: C, 48.98; H, 3.34; N, 3.57. Found: C, 48.22; H, 3.20; N, 3.57.

$[NBu_4][Pt(Me\text{-}thiazdt)_2]$. To dry MeOH (20 mL) under inert conditions, sodium metal (70 mg, 3.0 mmol) was added. The protected ligand **1**-Me (300 mg, 0.99 mmol) was then transferred to the mixture. After complete dissolution the solution was stirred for 30 min at room temperature. Then a solution of K_2PtCl_4 (210 mg, 0.5 mmol) and NBu_4Br (330 mg, 1.02 mmol) in pure water (10 mL) was added followed by 18 hours of stirring. The formed precipitate was filtered and recrystallized from chlorobenzene/acetone (80/20) at 0 °C to afford the monoanion $[NBu_4][Pt(Me\text{-}thiazdt)_2]$ as dark red brown crystals. Yield: 70% (290 mg); m.p. = 202 °C; MS (TOF MS ES−) calcd for $[C_8H_6N_2PtS_8]^{1-}$: 581.79. Found: 581.79; elem. anal. calcd for $[C_{24}H_{42}N_3PtS_8]$: C, 34.97; H, 5.14; N, 5.10; S, 31.12. Found: C, 34.94; H, 4.89; N, 5.06; S, 31.12.

$[NBu_4][Pt(Et\text{-}thiazdt)_2]$. To dry MeOH (20 mL) under inert conditions, sodium metal (34 mg, 1.5 mmol) was added. The protected ligand **1**-Et (150 mg, 0.47 mmol) was then transferred to the mixture. After complete dissolution the solution was stirred for 30 min at room temperature. Then a solution of K_2PtCl_4 (101 mg, 0.24 mmol) and NBu_4Br (170 mg, 0.52 mmol) in pure water (10 mL) was added followed by 18 hours of stirring. The formed precipitate was filtered and recrystallized from chlorobenzene/acetone 80/20 at 0 °C to afford the monoanionic complex $[NBu_4][Pt(Et\text{-}thiazdt)_2]$ as dark red brown crystals. Yield: 37% (75 mg); m.p. = 154 °C; MS (TOF MS ES−) calcd for $[C_{10}H_{10}N_2PtS_8]^{1-}$: 609.82. Found: 609.82; elem. anal. calcd for $C_{26}H_{46}N_3PtS_8$: C, 36.64; H, 5.44; N, 4.93; S, 30.10. Found: C, 36.12; H, 5.04; N, 4.68; S, 29.95.

Electrocrystallizations

They were systematically performed in two-compartment cells with Pt electrodes under inert atmosphere with degassed solvents. Albeit neutral complexes are obtained, the choice of the electrolyte added in the cell to lower its resistance is particularly important to favor a given phase and/or high-quality crystals.

$[Ni(Me\text{-}thiazdt)_2]$ (NiMe). Ph_4PCl (200 mg) dissolved in 10 mL of CH_2Cl_2/MeOH (7 : 2) was introduced in both compartments as supporting electrolyte. The nickel complex $[Ph_4P][Ni(Me\text{-}thiazdt)_2]$ (10 mg) was introduced in the anodic compartment. The current intensity was adjusted to 0.6 μA, and the reaction was left during seven days. Crystals of the neutral Ni complex $[Ni(Me\text{-}thiazdt)_2]$ were collected on the anode as long needles.

$[Ni(Et\text{-}thiazdt)_2]$ (NiEt). A monoclinic phase has been obtained earlier when using Et_4NBr as electrolyte, together with a few crystals of a triclinic phase that had escaped our attention at that time. The latter triclinic phase has been obtained here almost pure when using Et_4NPF_6 or Me_4NPF_6 as electrolyte, with the best crystals in the presence of Et_4NPF_6.

$[Pt(Me\text{-}thiazdt)_2]$ (PtMe). Bu_4NBF_4 (200 mg) and the platinum complex $[Bu_4N][Pt(Me\text{-}thiazdt)_2]$ (10 mg) were dissolved in 10 mL of CH_2Cl_2/CH_3CN (3/7). The current intensity was adjusted to 0.5 μA, and the current was maintained during five days. Crystals of the neutral Pt complex $[Pt(Me\text{-}thiazdt)_2]$ were collected on the anode.

$[Pt(Et\text{-}thiazdt)_2]$ (PtEt). Bu_4NBF_4 (200 mg) and the platinum complex $[Bu_4N][Pt(Et\text{-}thiazdt)_2]$ (10 mg) were dissolved in 15 mL of CH_3CN. The current intensity was adjusted to 0.5 μA, and the current was maintained during nine days. Crystals of the neutral Pt complex $[Pt(Et\text{-}thiazdt)_2]$ were collected on the anode as small needles.

X-ray crystallography

Data collections were performed on an APEXII Bruker-AXS diffractometer equipped with a CCD camera for $[Ph_4P][Ni(Me\text{-}thiazdt)_2]$, $[Ni(Me\text{-}thiazdt)_2]$ (**NiMe**) and $[Ni(Et\text{-}thiazdt)_2]$ (**NiEt**), on a D8 VENTURE Bruker AXS diffractometer for $[Ph_4P][Ni(Me\text{-}thiazdt)_2]{\cdot}CH_2Cl_2$, and on a XtaLAB AFC11 Rigaku diffractometer for $[Pt(Me\text{-}thiazdt)_2]$ (**PtMe**) and $[Pt(Et\text{-}thiazdt)_2]$ (**PtEt**). Structures were solved by direct methods using either the *SIR97* program,[29] and then refined with full-matrix least-square methods based on F^2 (SHELXL-97)[30] with the aid of the WINGX program.[31] All non-hydrogen atoms were refined with anisotropic atomic displacement parameters. H atoms were finally included in their calculated positions. Details of the final refinements are summarized in Table 4 for the radical anion species and in Table 5 for the neutral complexes.

First-principles density functional theory calculations

To study electronic structures of $[Ni(Me\text{-}thiazdt)_2]$ and tricl-$[Ni(Et\text{-}thiazdt)_2]$, we perform first principles calculations based on the density-functional theory.[32,33] One-electron Kohn–Sham equations are solved self-consistently by using a pseudopotential technique[34] with planewave basis sets adopting the projected augmented plane wave (PAW) method.[35] The structural relaxations under constant pressures are performed by calculating the stress tensors with a local density functional of generalized gradient approximation (GGA-PBE)[36] and a non-local electron correlation functional[37] (van der Waals density functional of vdw-df2-b86r),[38] which is implemented in a scalar relativistic code of Quantum Espresso 6.3.[39,40] The plane waves prepared with the cutoff energy

Table 4 Crystallographic data for anionic complexes

Compound	$[PPh_4][Ni(Me\text{-}thiazdt)_2]$	$[PPh_4][Ni(Me\text{-}thiazdt)_2]$, CH_2Cl_2	$[PPh_4][Pt(Et\text{-}thiazdt)_2]$, toluene
Formulae	$C_{32}H_{26}N_2NiPS_8$	$C_{32}H_{26}N_2NiPS_8$, CH_2Cl_2	$C_{34}H_{30}N_2PtPS_8$, C_7H_8
FW (g mol^{-1})	784.71	869.63	1041.27
System	Monoclinic	Orthorhombic	Monoclinic
Space group	$C2/c$	$P2_1ca$	$C2/c$
a (Å)	18.180(3)	22.3714(18)	26.190(3)
b (Å)	6.9147(11)	6.8300(6)	7.3028(7)
c (Å)	27.469(4)	24.2552(18)	24.991(2)
α (deg.)	90	90	90
β (deg.)	92.999(8)	90	115.389(3)
γ (deg.)	90	90	90
V (Å^3)	3448.4(9)	3706.1(5)	4318.1(7)
T (K)	296(2)	150(2)	296(2)
Z	4	4	4
D_{calc} (g cm^{-1})	1.511	1.559	1.602
μ (mm^{-1})	1.120	1.190	10.291
Total refls	14 792	28 970	34 302
Abs. corr.	Multiscan	Multiscan	Multiscan
Uniq. refls (R_{int})	3917 (0.0699)	7983 (0.0798)	4632 (0.0496)
Uniq. refls ($I > 2\sigma(I)$)	1964	6101	4230
R_1, wR_2	0.0499, 0.1215	0.0621, 0.1326	0.0454, 0.1044
R_1, wR_2 (all data)	0.1347, 0.1611	0.0948, 0.1485	0.0501, 0.1074
GOF	0.919	0.969	1.225

Table 5 Crystallographic data for neutral complexes

Compound	**NiMe**	tricl-**NiEt**	**PtMe**	**PtEt**
Formulae	$C_8H_6N_2NiS_8$	$C_{10}H_{10}N_2NiS_8$	$C_8H_6N_2PtS_8$	$C_{10}H_{10}N_2PtS_8$
FW (g mol^{-1})	445.32	473.39	581.72	609.77
System	Triclinic	Triclinic	Monoclinic	Triclinic
Space group	$P\bar{1}$	$P\bar{1}$	$P2_1/c$	$P\bar{1}$
a (Å)	4.2398(11)	5.987(2)	6.2481(11)	5.9582(5)
b (Å)	6.4701(14)	7.255(3)	4.6675(5)	7.2585(7)
c (Å)	13.666(3)	10.734(4)	25.802(5)	10.8670(8)
α (deg.)	93.863(6)	98.084(11)	90	98.508(7)
β (deg.)	96.356(7)	96.421(11)	94.826(18)	97.392(7)
γ (deg.)	90.152(6)	109.878(11)	90	109.362(8)
V (Å^3)	371.71(15)	427.7(3)	749.8(2)	430.49(7)
T (K)	296(2)	296(2)	293(2)	293(2)
Z	1	1	2	1
D_{calc} (g cm^{-1})	1.989	1.838	2.577	2.352
μ (mm^{-1})	2.411	2.101	10.454	9.110
Total refls	8252	8870	5906	4422
Abs. corr.	Multiscan	Multiscan	Multiscan	Multiscan
Uniq. refls (R_{int})	1717 (0.0722)	1955 (0.0347)	1807 (0.1020)	2008 (0.0656)
Uniq. refls ($I > 2\sigma(I)$)	1107	1628	1063	1713
R_1, wR_2	0.0438, 0.0808	0.0306, 0.0639	0.0984, 0.1514	0.0417, 0.1042
R_1, wR_2 (all data)	0.091, 0.0941	0.0445, 0.0732	0.1837, 0.1750	0.0489, 0.1087
GOF	0.981	1.112	1.112	0.704

of 65 and 70 Ry were used for NiMe and tricl-**NiEt**, respectively. Cutoff energies for electronic charge and potentials are set to be 588 and 488 Ry for **NiMe** and tricl-**NiEt**, respectively. Used uniform k-point meshes are 8 × 4 × 4 and 6 × 6 × 4 for NiMe and tricl-**NiEt**, respectively with a Gaussian smearing method during self-consistent loops.

Transport measurements

Single crystals of **NiMe** sample 1, tricl-**NiEt** and **PtMe** (with an average size of 0.15 × 0.02 × 0.015 mm^3) and **NiMe** sample (20.09 × 0.02 × 0.015 mm^3) were used for the high-pressure measurements. The sample was mounted in the DAC by using the same technique as that used for $[Ni(ptdt)_2]$.[41] The sample was encapsulated with a mixture of epoxy and alumina. The diamond with culet size of 0.7 mm and tension annealed stainless steel SUS301 were used for **NiMe** sample 1 and tricl-**NiEt**, and the diamond with culet size of 0.56 mm and Inconel 625 for **NiMe** sample 2. Electrical contacts were obtained by attaching four gold wires (ϕ 10 or 5 μm) with gold paint, and the four-probe DC method was used for all measurements. Daphne Oil 7373 was used as the pressure transmitting medium. The pressure was determined by the shift in the ruby fluorescence $R1$ lines at room temperature.

Conflicts of interest

There are no conflicts to declare.

Acknowledgements

This work was supported in part by Université de Rennes 1 (PhD grant to H. H.) and by the JSPS KAKENHI (Grant Numbers JP16K17756, JP19K21860, and JP16H06346). The stay of H. H. to RIKEN was supported in part by RIKEN International Program Associate and by Rennes Métropole. Their support is gratefully acknowledged. T. T. is partially supported by MEXT Japan, Leading Initiative for Excellent Young Researchers (LEADER). The computations were mainly carried out using the computer facilities of ITO at the Research Institute for Information Technology, Kyushu University, MASAMUNE at IMR, Tohoku University, and HOKUSAI-GreatWave at RIKEN, Japan.

Notes and references

1 S. K. Pal, M. E. Itkis, F. S. Tham, R. W. Reed, R. T. Oakley and R. C. Haddon, *Science*, 2005, **309**, 281–284.
2 S. Mandal, S. Samanta, M. E. Itkis, D. W. Jensen, R. W. Reed, R. T. Oakley, F. S. Tham, B. Donnadieu and R. C. Haddon, *J. Am. Chem. Soc.*, 2006, **128**, 1982–1994.
3 M. P. Andrews, A. W. Cordes, D. C. Douglass, R. M. Fleming, S. H. Glarum, R. C. Haddon, P. Marsh, R. T. Oakley, T. T. M. Palstra, L. F. Schneemeyer, G. W. Trucks, R. W. Tycko, J. V. Waszczak, K. M. Young and N. M. Zimmerm, *J. Am. Chem. Soc.*, 1991, **113**, 3559–3568.
4 A. W. Cordes, R. C. Haddon, R. G. Hicks, R. T. Oakley, T. T. M. Palstra, L. F. Schneemeyer and J. V. Waszczak, *J. Am. Chem. Soc.*, 1992, **114**, 1729–1732.
5 A. A. Leitch, R. W. Reed, C. M. Robertson, J. F. Britten, X. Yu, R. A. Secco and R. T. Oakley, *J. Am. Chem. Soc.*, 2007, **129**, 7903–7914.
6 D. Tian, S. M. Winter, A. Mailman, J. W. L. Wong, W. Yong, H. Yamaguchi, Y. Jia, J. S. Tse, S. Desgreniers, R. A. Secco, S. R. Julian, C. Jin, M. Mito, Y. Ohishi and R. T. Oakley, *J. Am. Chem. Soc.*, 2015, **137**, 14136–14148.
7 (*a*) H. Tanaka, Y. Okano, H. Kobayashi, W. Suzuki and A. Kobayashi, *Science*, 2001, **291**, 285; (*b*) A. Kobayashi, E. Fujiwara and H. Kobayashi, *Chem. Rev.*, 2004, **104**, 5243–5264.
8 (*a*) B. Zhou, Y. Idobata, A. Kobayashi, H. Cui, R. Kato, R. Takagi, K. Miyagawa, K. Kanoda and H. Kobayashi, *J. Am. Chem. Soc.*, 2012, **134**, 12724–12731; (*b*) B. Zhou, S. Ishibashi, T. Ishii, T. Sekine, R. Takehara, K. Miyagawa, K. Kanoda, E. Nishibori and A. Kobayashi, *Chem. Commun.*, 2019, **55**, 3327–3330; (*c*) H. Cui, H. Kobayashi, S. Ishibashi, M. Sasa, F. Iwase, R. Kato and A. Kobayashi, *J. Am. Chem. Soc.*, 2014, **136**, 7619–7622.
9 J. P. Nunes, M. J. Figueira, D. Belo, I. C. Santos, B. Ribeiro, E. B. Lopes, R. T. Henriques, J. Vidal-Gancedo, J. Veciana, C. Rovira and M. Almeida, *Chem. – Eur. J.*, 2007, **13**, 9841–9849.
10 (*a*) T. Isono, H. Kamo, A. Ueda, K. Takahashi, A. Nakao, R. Kumai, H. Nakao, K. Kobayashi, Y. Murakami and H. Mori, *Nat. Commun.*, 2013, **4**, 1344–1349; (*b*) A. Ueda, S. Yamada, T. Isono, H. Kamo, A. Nakao, R. Kumai, H. Nakao, Y. Murakami, K. Yamamoto, Y. Nishio and H. Mori, *J. Am. Chem. Soc.*, 2014, **136**, 12184–12192.
11 Y. Kobayashi, T. Terauchi, S. Sumi and Y. Matsushita, *Nat. Mater.*, 2017, **16**, 109–114.
12 (*a*) N. C. Schiødt, T. Bjørnholm, K. Bechgaard, J. J. Neumeier, C. Allgeier, C. S. Jacobsen and N. Thorup, *Phys. Rev. B: Condens. Matter Mater. Phys.*, 1996, **53**, 1773–1778; (*b*) A. J. Schultz, H. H. Wang, L. C. Soderholm, T. L. Sifter, J. M. Williams, K. Bechgaard and M. H. Whangbo, *Inorg. Chem.*, 1987, **26**, 3757–3761; (*c*) A. Filatre-Furcate, P. Auban-Senzier, M. Fourmigué, T. Roisnel, V. Dorcet and D. Lorcy, *Dalton Trans.*, 2015, **44**, 15683–15689.
13 (*a*) D. Belo, H. Alves, E. B. Lopes, M. T. Duarte, V. Gama, R. T. Henriques, M. Almeida, A. Perez-Benítez, C. Rovira and J. Veciana, *Chem. – Eur. J.*, 2001, **7**, 511–519; (*b*) T. Higashino, O. Jeannin, T. Kawamoto, D. Lorcy, T. Mori and M. Fourmigué, *Inorg. Chem.*, 2015, **54**, 9908–9913; (*c*) O. J. Dautel, M. Fourmigué, E. Canadell and P. Auban-Senzier, *Adv. Funct. Mater.*, 2002, **12**, 693–698; (*d*) D. G. Branzea, F. Pop, P. Auban-Senzier, R. Clérac, P. Alemany, E. Canadell and N. Avarvari, *J. Am. Chem. Soc.*, 2016, **138**, 6838–6851.
14 N. Tenn, N. Bellec, O. Jeannin, L. Piekara-Sady, P. Auban-Senzier, J. Íñiguez, E. Canadell and D. Lorcy, *J. Am. Chem. Soc.*, 2009, **131**, 16961–16967.
15 G. Yzambart, N. Bellec, G. Nasser, O. Jeannin, T. Roisnel, M. Fourmigué, P. Auban-Senzier, J. Íñiguez, E. Canadell and D. Lorcy, *J. Am. Chem. Soc.*, 2012, **134**, 17138–17148.
16 Y. Le Gal, T. Roisnel, P. Auban-Senzier, N. Bellec, J. Íñiguez, E. Canadell and D. Lorcy, *J. Am. Chem. Soc.*, 2018, **140**, 6998–7004.
17 L. Valade, J. P. Legros, M. Bousseau, P. Cassoux, M. Garbauskas and L. V. Interrante, *J. Chem. Soc., Dalton Trans.*, 1985, 783–794.
18 B. Garreau-de Bonneval, K. I. M.-C. Ching, F. Alary, T.-T. Bui and L. Valade, *Coord. Chem. Rev.*, 2010, **254**, 1457–1467.
19 H. Cui, T. Tsumuraya, T. Miyazaki, Y. Okano and R. Kato, *Eur. J. Inorg. Chem.*, 2014, 3837–3840.
20 A. Filatre-Furcate, N. Bellec, O. Jeannin, P. Auban-Senzier, M. Fourmigué, A. Vacher and D. Lorcy, *Inorg. Chem.*, 2014, **53**, 8681–8690.
21 S. Eid, M. Fourmigué, T. Roisnel and D. Lorcy, *Inorg. Chem.*, 2007, **46**, 10647–10654.
22 M. C. Aragoni, M. Arca, F. A. Devillanova, F. Isaia, V. Lippolis, A. Mancini, L. Pala, A. M. Z. Slawin and J. D. Woollins, *Inorg. Chem.*, 2005, **44**, 9610–9612.
23 K. W. Browall, T. Bursh, L. V. Interrante and J. S. Kasper, *Inorg. Chem.*, 1972, **11**, 1800–1806.
24 V. V. Gritsenko, O. A. D'yachenko, P. Cassoux, A. I. Kotov, E. E. Laukhina, C. Faulmann and E. B. Yagubskii, *Russ. Chem. Bull.*, 1993, **42**, 1149–1151.
25 E. Kogut, J. A. Tang, A. J. Lough, C. M. Widdifield, R. W. Schurko and U. Fekl, *Inorg. Chem.*, 2006, **45**, 8850–8852.
26 C. Deiana, M. C. Aragoni, F. Isaia, V. Lippolis, A. Pintus, A. M. Z. Slawin, J. D. Woollins and M. Arca, *New J. Chem.*, 2016, **40**, 8206–8210.
27 M. Dion, H. Rydberg, E. Schröder, D. C. Langreth and B. I. Lundqvist, *Phys. Rev. Lett.*, 2004, **92**, 246401.

28 M. Kawamura, *Comput. Phys. Commun.*, 2019, **239**, 197–203.
29 A. Altomare, M. C. Burla, M. Camalli, G. Cascarano, C. Giacovazzo, A. Guagliardi, A. G. G. Moliterni, G. Polidori and R. Spagna, *J. Appl. Crystallogr.*, 1999, **32**, 115–119.
30 G. M. Sheldrick, *Acta Crystallogr., Sect. A: Found. Crystallogr.*, 2008, **64**, 112–122.
31 L. J. Farrugia, *J. Appl. Crystallogr.*, 2012, **45**, 849–854.
32 P. Hohenberg and P. W. Kohn, *Phys. Rev.*, 1964, **136**, B864–B871.
33 W. Kohn and L. J. Sham, *Phys. Rev.*, 1965, **140**, 1133–1138.
34 D. Vanderbilt, *Phys. Rev. B: Condens. Matter Mater. Phys.*, 1990, **41**, 7892–7895.
35 P. Blöchl, *Phys. Rev. B: Condens. Matter Mater. Phys.*, 1994, **50**, 17953–17979.
36 J. P. Perdew, K. Burke and M. Ernzerhof, *Phys. Rev. Lett.*, 1996, **77**, 3865–3868.
37 R. Sabatini, E. Kucukbenli, B. Kolb, T. Thonhauser and S. de Gironcoli, *J. Phys.: Condens. Matter*, 2012, **24**, 424209.
38 I. Hamada, *Phys. Rev. B: Condens. Matter Mater. Phys.*, 2014, **89**, 121103. Erratum: *Phys. Rev. B: Condens. Matter Mater. Phys.*, 2015, **91**, 119902.
39 P. Giannozzi, *et al.*, *J. Phys.: Condens. Matter*, 2009, **21**, 395502.
40 P. Giannozzi, *et al.*, *J. Phys.: Condens. Matter*, 2017, **29**, 465901.
41 H. Cui, J. S. Brooks, A. Kobayashi and H. Kobayashi, *J. Am. Chem. Soc.*, 2009, **131**, 6358–6359.